JGR Atmospheres

Supporting Information for

Optimizing the isoprene emission model MEGAN with satellite and ground-based observational constraints

Christian A. DiMaria[1*], Dylan B. A. Jones[1], Helen Worden[2], A. Anthony Bloom[3], Kevin Bowman[3], Trissevgeni Stavrakou[4], Kazuyuki Miyazaki[3], John Worden[3], Alex Guenther[5], Chinmoy Sarkar[6†], Roger Seco[7], Jeong-Hoo Park[8], Julio Tota[9], Eliane Gomes Alvez[10], and Valerio Ferracci[11]

[1]Department of Physics, University of Toronto, Toronto, Ontario, Canada, [2]Atmospheric Chemistry Observations & Modeling Laboratory, National Center for Atmospheric Research, Boulder, CO, USA, [3]Jet Propulsion Laboratory, California Institute of Technology, Pasadena, CA, USA, [4]Royal Belgian Institute for Space Aeronomy (BIRA-IASB), Brussels, Belgium, [5]Department of Earth System Science, University of California, Irvine, CA, USA, [6]Air Quality Research Center, University of California, Davis, CA, USA, [7]Institute of Environmental Assessment and Water Research (IDAEA-CSIC), Barcelona, Catalonia, Spain, [8]Air Quality Reserach Division, National Institute of Environmetal Research, 22689, Republic of Korea, [9]Julio Tota, Instituto de engenharia e Geociências, Universidade Federal do Oeste do Pará, UFOPA, Santarém, Pará, Brazil, [10]Department of Biogeochemical Processes, Max Planck Institute for Biogeochemistry, Jena, Germany, [11]School of Water, Energy and Environment, Cranfield University, Cranfield, UK

Corresponding author: Christian DiMaria (christian.dimaria@mail.utoronto.ca)

† Now at Thermo Fisher Scientific, San Francisco, CA, USA

Contents of this file

Text S1. MEGAN normalization with canopy environment coefficient

The canopy environment coefficient C_{CE} is a normalization constant which ensures that $E_{ISOP} = E_0$ under standard conditions. These conditions are listed in Table S1. The normalization constant is defined as

$$C_{CE} = \frac{1}{(\gamma_T \times \gamma_{PAR} \times \gamma_{LAI} \times \gamma_{AGE} \times \gamma_{CO2} \times \gamma_{SM})_{Std}} \quad \text{(S1)}$$

where the subscript *Std* indicates that each $\boldsymbol{\gamma}$-factor is calculated at standard conditions. The definition of C_{CE} makes it sensitive to certain $\boldsymbol{\gamma}_T$ parameters, including T_{Max}, C_{T1}, and C_{T2}, while it is insensitive to other parameters including K_1 and K_2. The $\boldsymbol{\gamma}_T$ parameter C_{EO} has no impact on MEGAN isoprene emissions because it appears as a multiplicative factor in $\boldsymbol{\gamma}_T$ and in $\boldsymbol{\gamma}_{T,Std}$ (i.e., in both the numerator and denominator of the MEGAN equation). Because C_{CE} is sensitive to the values of the $\boldsymbol{\gamma}_T$ parameters, we multiply our posterior $\boldsymbol{\gamma}_T$ by the updated normalization constant when calculating posterior MEGAN

emissions. This is necessary to ensure $E_{ISOP} = E_0$ under standard conditions when using the posterior parameterization. All plots of γ_T in the main text are thus multiplied by their corresponding C_{CE} values (i.e., either the a priori or posterior C_{CE}) to ensure they are all normalized to the same standard conditions.

Text S2. Long term temperature response in MEGAN γ_T

The MEGAN temperature response γ_T exhibits hysteresis with respect to past ambient temperatures. Emissions increase up with temperature up to an optimal value E_{Opt}, given by

$$E_{Opt} = \left[C_{EO} \times \exp\left(K_2\left(T_{daily} - 297\right)\right)\right], \quad \text{(S2)}$$

which occurs at temperature T_{Opt}, given by

$$T_{Opt} = T_{Max} + \left(K_1\left(T_{daily} - 297\right)\right) \quad \text{(S3)}$$

where C_{EO} is a scaling factor, T_{Daily} is the ambient temperature (in K) of the past 24 hours, T_{Max} (313 K) is the standard optimal temperature, and K_1 (0.6) and K_2 (0.08) are coefficients which determine the sensitivity of E_{Opt} and T_{Opt} to variations in T_{Daily} (Guenther et al., 2006). Values of T_{Daily} greater than 297 K will increase the optimum value of γ_T (E_{Opt}) as well as cause this optimum to occur at a higher temperature (T_{Opt}). The opposite occurs when T_{Daily} falls below 297 K. The magnitude of these changes in E_{Opt} and T_{Opt} is set by K_1 and K_2, with larger values of these parameters giving a higher sensitivity to T_{Daily} and vice versa. These impacts are illustrated in Figure S1.

This algorithm is based on a limited number of experiments (Geron et al., 2000; Hanson & Sharkey, 2001; Monson et al., 1994; Pétron et al., 2001), leading to relatively large uncertainties in the empirical parameters C_{EO}, T_{Max}, K_1, and K_2. We therefore treat these as free parameters in our optimization experiments. However, the parameter C_{EO} has no impact on modelled emissions when γ_T is used within the full MEGAN equation (Equation (1) in the main text) due to the normalization of emissions to E_0 under standard environmental conditions (see Supplementary Text S1).

Text S3. Sensitivity of E_0 optimization to observation errors

In our top-down optimization of E_0 we assumed a constant relative error in the observations of 30%. This is consistent with early OMI-based top-down emission inventories (Millet et al., 2006). It is possible that we are overestimating the uncertainty in some regions, but we are likely underestimating it in others, due to spatially and temporally varying sources of error in the satellite-derived products (including CH_2O retrieval biases (Vigouroux et al., 2020; De Smedt et al., 2021), chemistry-transport model errors (Barkley et al., 2013; Stavrakou et al., 2015), spatial smearing errors (Palmer et al., 2003; Turner et al., 2012), and background CH_2O sources (Marais et al., 2012; Wolfe et al., 2016)). We therefore had to account for the potential impact of our uncertainty assumption on the optimization of E_0.

The optimization of model parameters is dependent on the accuracy and precision of the observational constraints. While we assume observations are unbiased during our experiments, we account for the precision (i.e., measurement noise and other random errors) of the observations explicitly in our MHMCMC scheme through the model likelihood function

$$P(\boldsymbol{x}_i) = \exp\left(-0.5\sum\left(\frac{(\boldsymbol{M}(\boldsymbol{x}_i) - \boldsymbol{O})^2}{\sigma_O^2}\right)\right), \quad \text{(S4)}$$

where $\boldsymbol{M}(\boldsymbol{x}_i)$ is the model output vector (in our case MEGAN isoprene emissions), $\boldsymbol{O}$ is the observation vector, and $\boldsymbol{\sigma}_O$ is the observation error. The presence of $\boldsymbol{\sigma}_O$ in the denominator of Equation (S4) ensures that more precise observations will give a more strongly peaked probability distribution and therefore stronger constraints on the model parameters.

We performed a series of simulated observation experiments to test the sensitivity of the E_0 optimization to the assumed observation error $\boldsymbol{\sigma}_O$. MEGAN was used to generate a "true" isoprene emission time series which was then sampled at user-specified intervals (hourly, daily, and monthly) and perturbed with Gaussian noise ($\boldsymbol{\sigma}_O$ = 1 % – 50%) to produce pseudo-observations. The pseudo-observations were then used to constrain E_0 in the MHMCMC scheme. Figure S2 shows a sample of how the posterior E_0 distribution changes as a function of observation frequency and error. Figure S2 (a) and (b) show the posterior E_0 as constrained with monthly observations with 5% and 25% error, respectively, while Figure S2 (c) and (d) show the results for hourly observations with the same errors as (a) and (b). The observation frequency had no significant impact on the optimization of E_0, whereas larger observation errors resulted in a broader posterior E_0 distribution. Despite the weaker constraints on E_0 with larger observation errors, the median posterior value is still well-within one standard deviation of the true E_0. The optimization was consistently able to recover E_0 up to an observation error of nearly 50%, at which point signal-to-noise was insufficient to constrain the emissions.

These simulated observation experiments suggest that top-down emission estimates are sufficiently precise to constrain E_0, and that our assumption of a 30% error has little impact on the posterior E_0 values other than potentially over or underestimating the standard deviation of the posterior E_0 distribution. This is a relatively minor issue when compared to other sources of error in the E_0 optimization, including the impact of drought stress, model input uncertainties, and discrepancies between different observation datasets (see main text Section 4).

Text S4. Mapping locally measured PAR to GEOS-FP PAR

Local PAR measurements are available at Wytham Woods in September 2018 but they are not available during the pre-heatwave period (25 May – 21 June). We consequently used hourly GEOS-FP PAR at 0.25° × 0.325° spatial resolution to drive MEGAN in our optimization experiments. To avoid introducing biases due to discrepancies between the local PAR measurements and the GEOS-FP PAR, we generated a linear mapping between the two datasets for September 2018 following the methodology of Ferracci et al (2020). This mapping is shown in Figure S3, in units of photosynthetic photon flux density (PPFD). There is a strong correlation between the local WIsDOM measurements and the GEOS-FP values (r^2 = 0.83). However, there is also a ~30% offset between the two datasets as indicated by the slope of the linear map in Figure S3, with WIsDOM PPFD measurements being consistently lower than the concurrent GEOS-FP values. We applied the linear map in Figure S3 to the pre-heatwave (25

May– 21 June) GEOS-FP PPFD data to account for this offset, effectively transforming the GEOS-FP PPFD into the local measurement space.

The linear map in Figure S3 is a source of error in our optimization, partially due to the large amount of scatter in the measurements and partially due to our assumption that a map based on September 2018 observations is applicable during the pre-heatwave period (25 May – 21 June). The impact of this source of error is limited by filtering the WIsDOM measurements for PPFD > 650 µmol/m^2/s (equivalent to PAR > 136 W/m^2). This effectively limits our observations to mid-day scenes (roughly 10am – 4pm local time, depending on cloud cover) and greatly reduces the sunlight-driven variability of the isoprene measurements. This is described in more detail in Section 3.2 of the main text, as well as in Ferracci et al (2020).

Text S5. Sensitivity of $\boldsymbol{\gamma}_T$ optimization to observation errors

We performed a series of simulated observation experiments to test the sensitivity of the $\boldsymbol{\gamma}_T$ optimization to the assumed observation error $\boldsymbol{\sigma}_O$. In these simulated observation experiments, MEGAN was used to generate a "true" isoprene emission time series which was then sampled at user-specified intervals (hourly, daily, and monthly) and perturbed with Gaussian noise ($\boldsymbol{\sigma}_O$ = 1 % – 50%) to produce pseudo-observations. The pseudo-observations were then used to constrain the $\boldsymbol{\gamma}_T$ parameters in the MHMCMC scheme. All 31 unique combinations of the $\boldsymbol{\gamma}_T$ parameters T_{Max}, K_1, K_2, C_{T1}, and C_{T2} were tested. For brevity, we present here only the results for the optimization of T_{Max} with all other parameters fixed to their a priori values.

Figure S4 shows how the posterior T_{Max} distribution changes as a function of observation error and observation frequency. The MHCMC can constrain T_{Max} given hourly observations with 1% relative error, resulting in a very narrow probability distribution (Figure S4 (a)). Increasing the observation error to 5% results in a much broader probability distribution and an incorrect median posterior value (Figure S4 (b)), though the mode of the distribution still coincides with the true parameter value. With an observation error of 25% the MHMCMC is unable to constrain T_{Max} even with hourly observations (Figure S4 (c)). Unlike with the E_0 optimization (Figure S2), the optimization of the $\boldsymbol{\gamma}_T$ parameters was sensitive to observation frequency. Figure S4 (d) shows that monthly observations with 1% error can constrain T_{Max}, but the probability distribution is broader than with hourly observations (Figure S4 (a)). T_{Max} could not be constrained with monthly observations with 5% error or greater (Figure S4 (e) and (f)).

None of the 31 combinations of $\boldsymbol{\gamma}_T$ parameters could be reliably constrained with observation errors exceeding 20% in our simulated observation experiments. This effectively ruled out the use of top-down isoprene emission estimates as constraints on $\boldsymbol{\gamma}_T$. Because of this, we only attempted to optimize $\boldsymbol{\gamma}_T$ using the BR-Sa1 eddy covariance flux measurements (observation error of ~15%; Sarkar et al., 2020) and WIsDOM isoprene mixing ratio measurements (observation error of ~10%; Ferracci et al., 2020).

Text S6. Sensitivity of MEGAN to E_0 and $\boldsymbol{\gamma}_T$ parameters

MEGAN has a different sensitivity to each of its empirical parameters, defined here as the change in model output for a given perturbation to an empirical parameter. This has important

implications for optimizing MEGAN parameters with observations using MHMCMC, because higher sensitivity parameters can be more readily constrained due to their larger impact on model output (i.e., perturbations to these parameters by the MHMCMC algorithm are more likely to produce a signal in the model output which rises above the noise in the observational constraints). Conversely, lower sensitivity parameters can only be constrained with more precise observations.

The sensitivity of MEGAN to E_0 and each of the $\boldsymbol{\gamma}_T$ parameters (T_{Max}, K_1, K_2, C_{T1}, and C_{T2}) is illustrated in Figure S5 (note that the $\boldsymbol{\gamma}_T$ parameter C_{EO} was omitted due to the normalization of MEGAN described in Supplementary Text S1). Each panel in Figure S5 shows the mean isoprene emission rate at BR-Sa1 from 1 – 16 June 2014 as calculated with MEGAN 2.1. The red circle in each panel represents the unperturbed emissions, using the a priori (PCEEA) value parameter values and the measured mean temperature at BR-Sa1 (this measured temperature is indicated by the vertical dotted black line). Deviations from this point on the y-axis represent perturbations to the MEGAN parameters, while deviations along the x-axis represent perturbations to the ambient daily temperature. The solid black contours represent the measured mean isoprene emission rate at BR-Sa1 ± 5 %.

By following the dotted black line from the red circle to the solid black contours in each panel, we can see that MEGAN could be brought into agreement with the BR-Sa1 observations (at least in terms of the mean emission rate for the whole time series) by: (a) increasing E_0 from 1 to 1.2 (in units of 10^9 kgC/m^2/s); (b) reducing T_{Max} from 313 K to 303 K; (c) reducing K_1 from 0.6 – 0.3; (d) increasing K_2 from 0.08 – 0.11; (e) reducing C_{T1} from 80 – 40 kJ/mol; or (f) reducing C_{T2} from 200 – 100 kJ/mol. The gradient along each path is a measure of the sensitivity of MEGAN to each parameter, with steeper gradients (e.g., E_0, K_2) indicating a higher sensitivity and shallower gradients (e.g., T_{Max}, K_1, C_{T1}, C_{T2}) indicating a lower sensitivity. This is illustrated in Figure S6, where we have used MEGAN 2.1 to calculate weekly mean isoprene emissions for 2014 in the Western Sahel regions with large perturbations to each of the MEGAN parameters. Large perturbations in E_0 (called "AEF" = "annual emission factor" in Figure S6) and K_2 lead to significant changes to the modelled emissions, while perturbations to K_1, T_{Max}, C_{T1}, and C_{T2} have a more minor impact. These sensitivities vary in time due to changes in ambient temperature; this is the same effect as is visible in Figure S5, where the gradient along the y-axis (i.e., parameter perturbation axis) changes as a function of position along the x-axis (i.e., the temperature axis).

These sensitivities are a proxy for our ability to constrain each parameter with observations, indicating that most of the $\boldsymbol{\gamma}_T$ parameters (except for K_2) are more difficult to constrain than E_0. However, it must be noted that the joint sensitivities which emerge when optimizing multiple MEGAN parameters simultaneously are not necessarily the same as those shown in Figure S5 or S6 where parameters were perturbed in isolation. It was therefore necessary to test all possible combinations of parameters in our optimization experiments to determine which subsets could be reasonably well constrained (see Supplementary Text S5).

Text S7. Optimization of T_{Max} and K_1 at BR-Sa1 using eddy covariance fluxes

There are 31 unique combinations of the 5 $\boldsymbol{\gamma}_T$ parameters T_{Max}, K_1, K_2, C_{T1}, and C_{T2}. Due to the differing sensitivity of MEGAN to each of these parameters, particularly when multiple

parameters are perturbed simultaneously, all 31 combinations were tested in our MHMCMC optimization to identify the best possible subset. Here "best" refers to the largest subset in which each parameter is reliably constrained while also significantly improving model-observation agreement. The γ_T parameter subset K_2, C_{T1}, and C_{T2} was identified as the best subset at BR-Sa1 using eddy covariance flux constraints (see Main Text Figure 7 and Figure 8). Many subsets contained poorly constrained parameters, or alternatively they contained well-constrained parameters but failed to significantly improve model-observation agreement.

Figure S7 shows the optimization results for the subset of T_{Max} and K_1 (the two empirical parameters in Equation S2). The posterior γ_T is extremely similar to the a priori over the range of observed temperatures and is not in significantly better agreement with the observations. Furthermore, the interquartile range of the posterior γ_T shows that T_{Max} and K_1 have a negligible impact on γ_T at lower temperatures but a very large impact at high temperatures. This is expected from Equation S2, as both parameters simply modulate the location of the high-temperature emission peak. The histograms in Figure S7 show that neither parameter is well-constrained by the optimization; the MHMCMC can effectively rule out a reduction in T_{Max} but is unable to distinguish between higher values of T_{Max} due to the low and asymmetric sensitivity of MEGAN to this parameter (see Figure S5 (b)). The K_1 parameter is dragged towards zero by the optimization, which reduces the model's sensitivity to T_{Daily} and keeps the emission peak closer to T_{Max}. This has the net effect of slightly increasing modelled emissions by moving the emission peak T_{Opt} closer to ambient temperatures, thereby slightly reducing model biases relative to the observations.

While the median posterior parameter values indicated in Figure S7 do reduce model biases (Figure S8 (a)), they do not improve the temporal variability of the estimate (i.e., the correlation between the model and the observations as indicated by the r^2 values in Figure S8 (b)). This contrasts with the subset of K_2, C_{T1}, and C_{T2} shown in the main text (Figure 8).

Text S8. Variability of MEGAN sensitivity T and LAI input errors

MEGAN isoprene emissions are highly sensitive to temperature due to the exponential form of γ_T over typical terrestrial temperature ranges (see Figure 11 in the main text). As a result, small errors in the temperature data used to drive MEGAN can lead to large errors in the modelled emissions. This can be seen in Figure S9 (a), which shows the relative change in seasonally averaged (December-January-February, 2016–2017) MEGAN isoprene emissions when positively biased temperature data are used to drive the model. A 1% temperature bias leads to emission biases in excess of 40% in most regions, consistent with our findings at BR-Sa1 when comparing the MERRA2 and locally measured temperature data (see Figure 5 (c) and (d) in the main text). From the viewpoint of model parameter optimization, it is clear that accurate temperature data must be used to drive MEGAN to obtain reliable emissions estimates and posterior parameters in all regions.

The sensitivity of MEGAN to LAI is much more variable, being high in low-LAI environments like the Sahel and negligible in high-LAI environments like the Amazon (see Figure 11 in the main text). This spatial variability is a direct consequence of the functional form of γ_{LAI} (Guenther et al., 2006),

$$\gamma_{LAI} = \frac{0.49LAI}{\sqrt{1 + 0.2LAI^2}} \quad \text{(S5)}$$

and is illustrated in Figure S9 (b),which shows the relative change in seasonally averaged (Dec-Jan-Feb) MEGAN isoprene emissions when positively biased LAI data are used to drive the model. The season Dec-Jan-Feb was chosen because this coincides with the minimum of the MODIS 8-Day LAI product in the Sahel of North Africa, allowing the spatial variability of LAI sensitivity in North African to be more easily seen. A 5% LAI bias leads to a 5% emission bias in the savannas of Northern and Southern Africa as well as Western Australia but has barely any impact (<1%) on emissions in tropical rainforest environments such as the Amazon or Congo River basins. Note that the large relative impact at high Northern latitudes in Figure S9 (b) is small in absolute terms, as total isoprene emissions from these regions are very low during boreal winter. The low sensitivity of MEGAN to LAI in forested regions implies that errors in LAI inputs are a likely only a very minor source of error (a few percent at most) in our model optimization in the Eastern Amazon, the Southeast US, and the UK temperate forest at Wytham Woods. On the other hand, LAI input errors may be on the order of 10% in the Western Sahel and Eastern Australia given the estimated uncertainty in the MODIS 8-day LAI product (Fang et al., 2013) and the higher sensitivity of MEGAN to LAI in low-LAI environments.

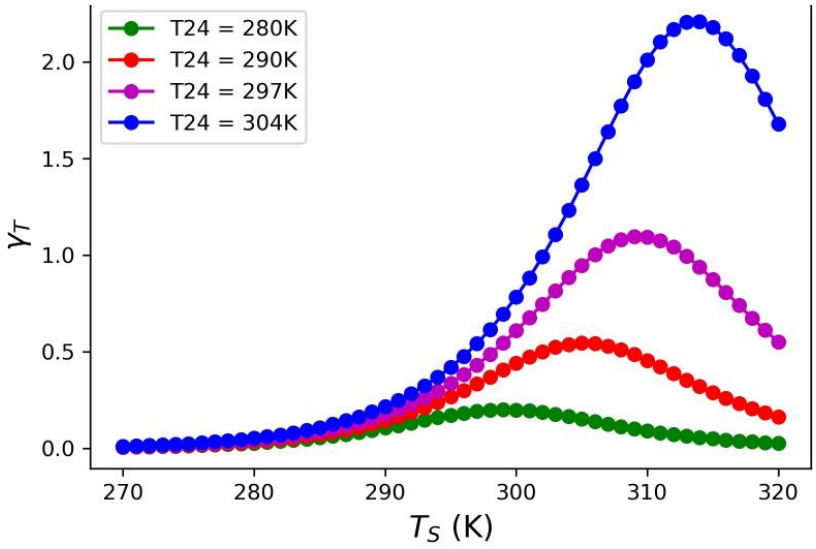

Figure S1. MEGAN temperature response γ_T plotted as a function of temperature for 4 different 24-hour average temperatures (T24, equivalent to T_{Daily} in Equation (S1) and (S2)). The standard value of T24 is 297 K, such that γ_T = 1 at 303 K (standard instantaneous temperature) and the emission peak is located at T_{Max} = 313 K. Changing the past ambient temperature changes both the location and height of the γ_T peak. The magnitude of these changes is controlled by K_1 and K_2 in Equation (S1) and (S2).

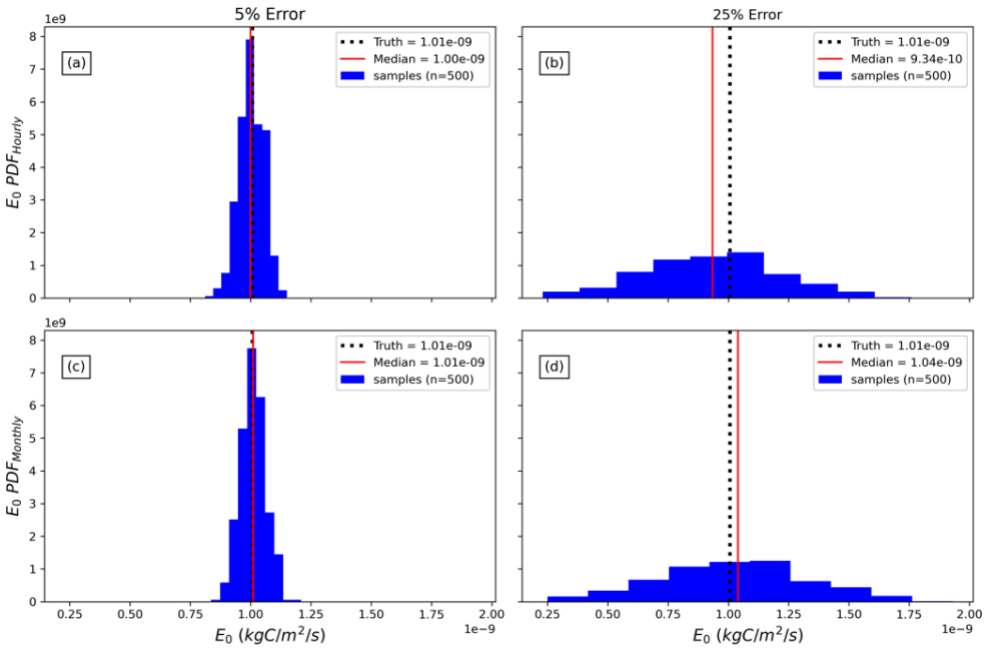

Figure S2. Posterior E_0 distribution for a selection of simulated observation experiments using 2014 MEGAN isoprene emissions in the Eastern Amazon region as the truth. The observation characteristics were (a) hourly with 5% error, (b) hourly with 25% error, (c) monthly with 5% error, and (d) monthly with 25% error. The true E_0 value is represented by the solid black line and the median posterior E_0 for each experiment is the solid red line. The blue histograms show a subsample of 500 E_0 values from the MHMCMC output (out of 5000 total accepted samples), which represents the posterior E_0 probability distribution.

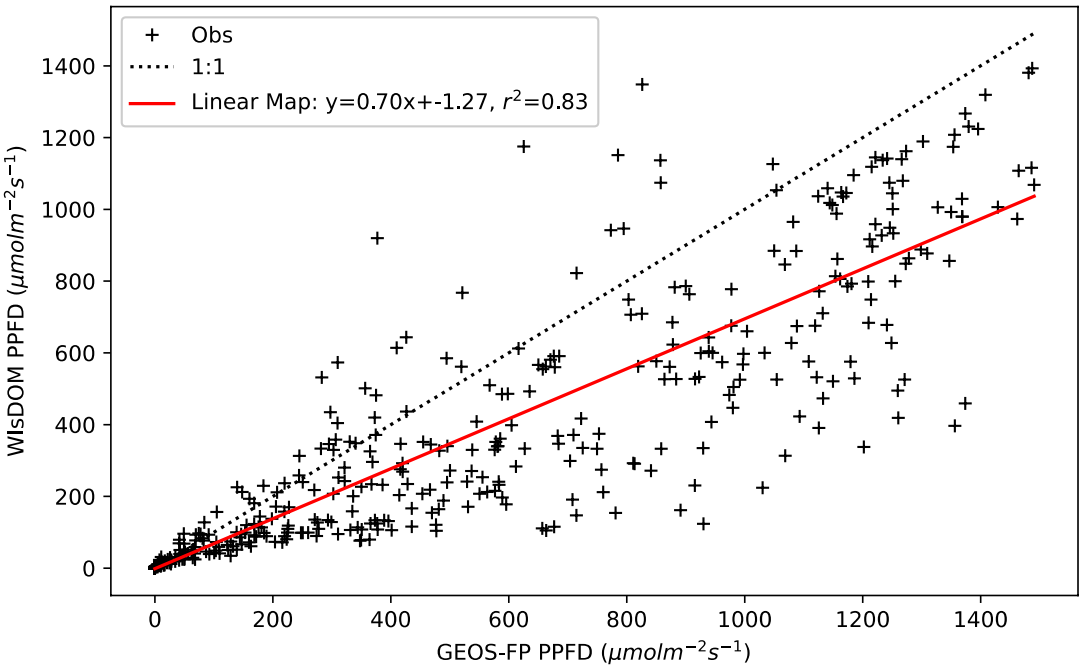

Figure S3. Scatter plot of local PAR measurements with GEOS-FP PAR for September 2018. The linear mapping (red line) was used to account for the systematic bias between the GEOS-FP PAR and the locally measured PAR in September 2018, and then applied to the GEOS-FP PAR during the pre-heatwave period.

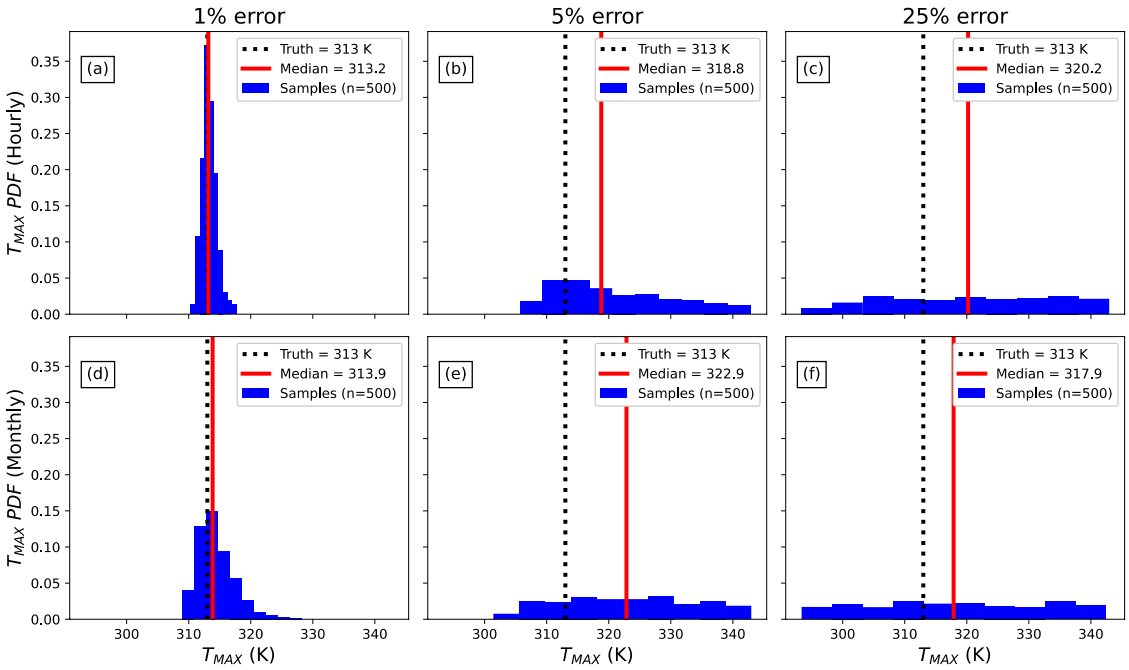

Figure S4. Posterior T_{Max} distribution for a selection of simulated observation experiments using 2014 MEGAN isoprene emissions in the Eastern Amazon region as the truth. The observation characteristics were (a) hourly with 1% error, (b) hourly with 5% error, (c) hourly with 25% error, (d) monthly with 1% error, (e) monthly with 5% error, and (f) monthly with 25% error. The true T_{Max} value is represented by the solid black line and the median posterior T_{Max} for each experiment is the solid red line. The blue histograms show a subsample of 500 T_{Max} values from the MHMCMC output (out of 5000 total accepted samples), which represents the posterior T_{Max} probability distribution.

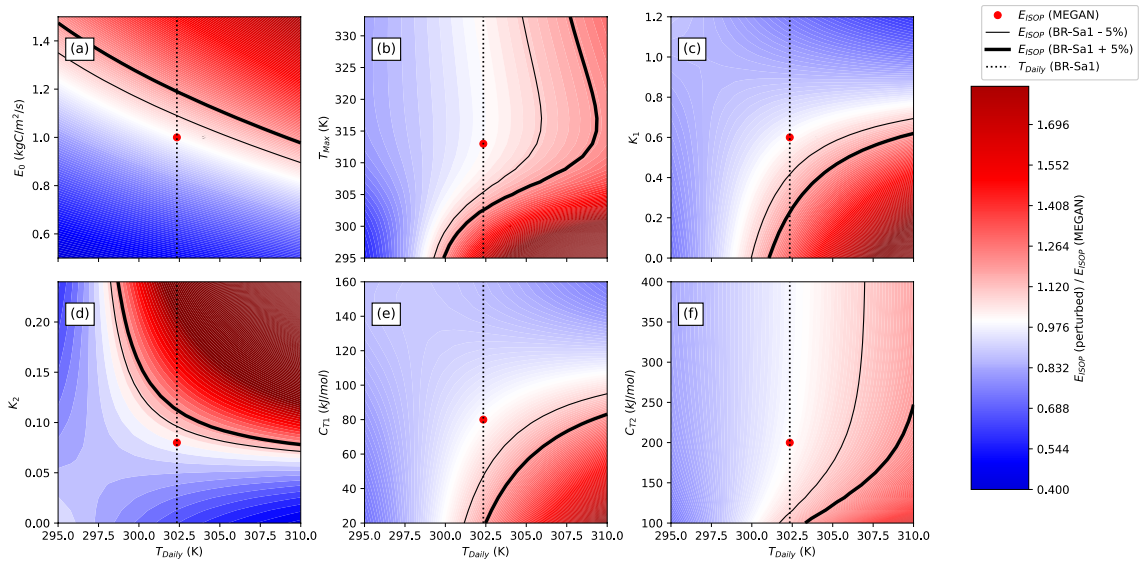

Figure S5. Sensitivity of mean MEGAN isoprene emissions at BR-Sa1 from 1 - 16 June 2014 to (a) E_0, (b) T_{Max}, (c) K_1, (d) K_2, (e) C_{T1}, and (f) C_{T2}. The red circle indicates the unperturbed MEGAN emissions, and the dashed vertical black line indicates the measured daily average temperature T_{Daily}. The y-axis of each panel shows parameter values, while the x-axis shows perturbations to the daily average temperature to illustrate the temperature dependence of the parameter sensitivity. The sensitivity is indicated by the gradient of each contour plot. The solid black lines indicate the average measured isoprene emission rate at BR-Sa1 ± 5 %.

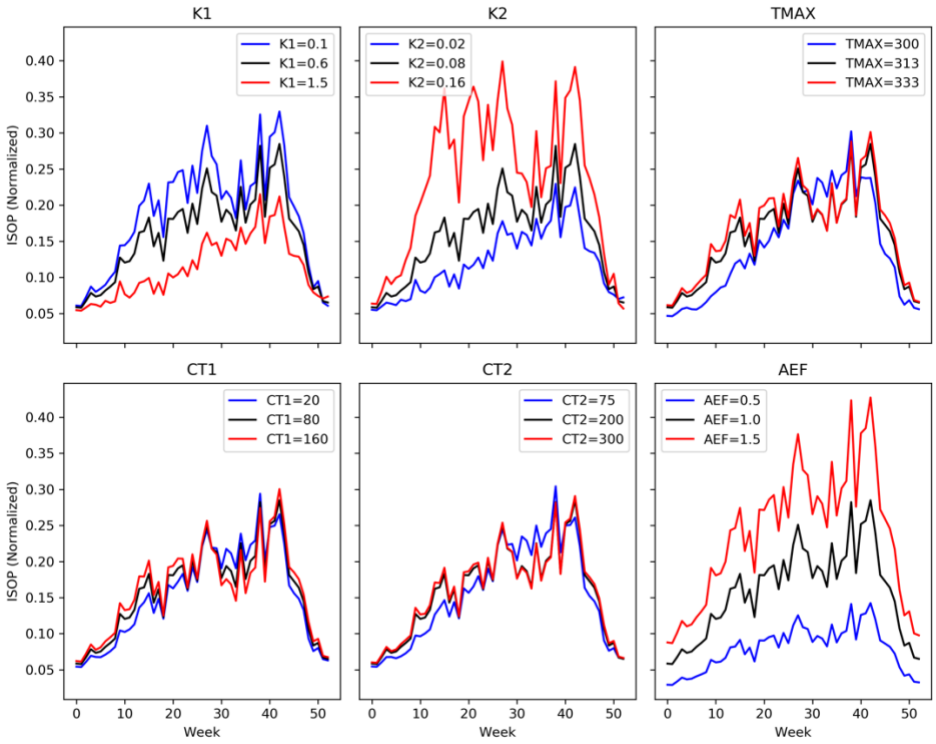

Figure S6. Weekly average isoprene emission rates (2014) in the Western Sahel region as calculated with MEGAN 2.1 using default (PCEEA) parameter values, normalized by AEF (note that AEF is equivalent to E_0). Positive (red) and negative (blue) perturbations to each parameter have an impact on the modelled emissions, with higher sensitivity parameters (AEF, K_2) impacting the emissions more than lower sensitivity parameters (K_1, T_{Max}, C_{T1}, C_{T2}).

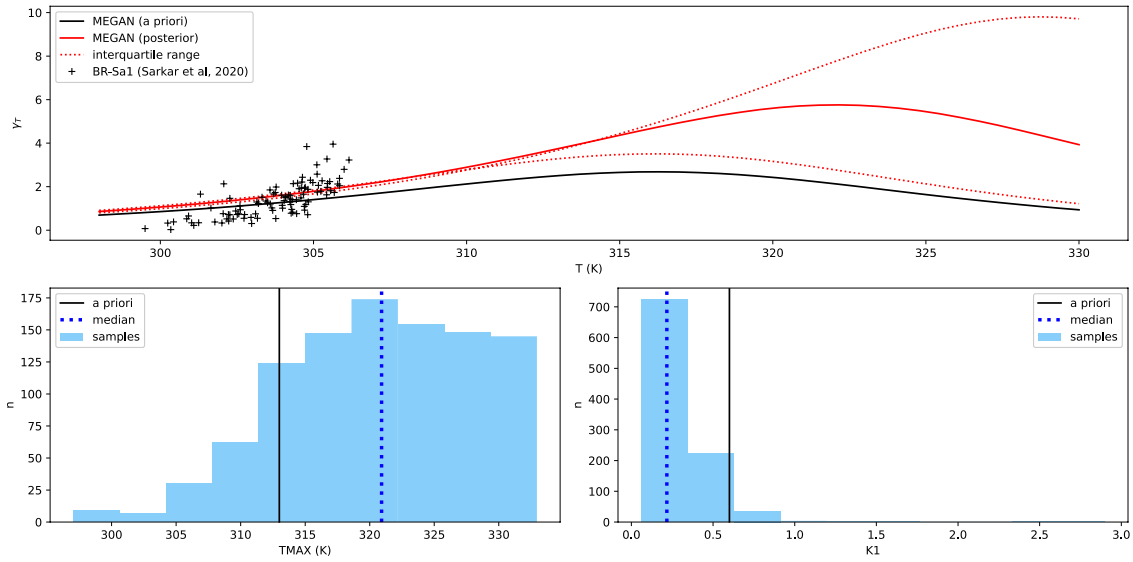

Figure S7. (top) A priori MEGAN $\boldsymbol{\gamma}_T$ (black), median posterior $\boldsymbol{\gamma}_T$ (solid red) and interquartile range (dotted red) as a function of temperature compared with the observed $\boldsymbol{\gamma}'_T$ (+ symbols) at BR-Sa1. Posterior parameter distributions for T_{Max} and K_1 are shown in the lower left and lower right panels, respectively (light blue). The median posterior values are indicated by the dashed blue lines in the lower panels, while the a priori values are indicated by the solid black lines.

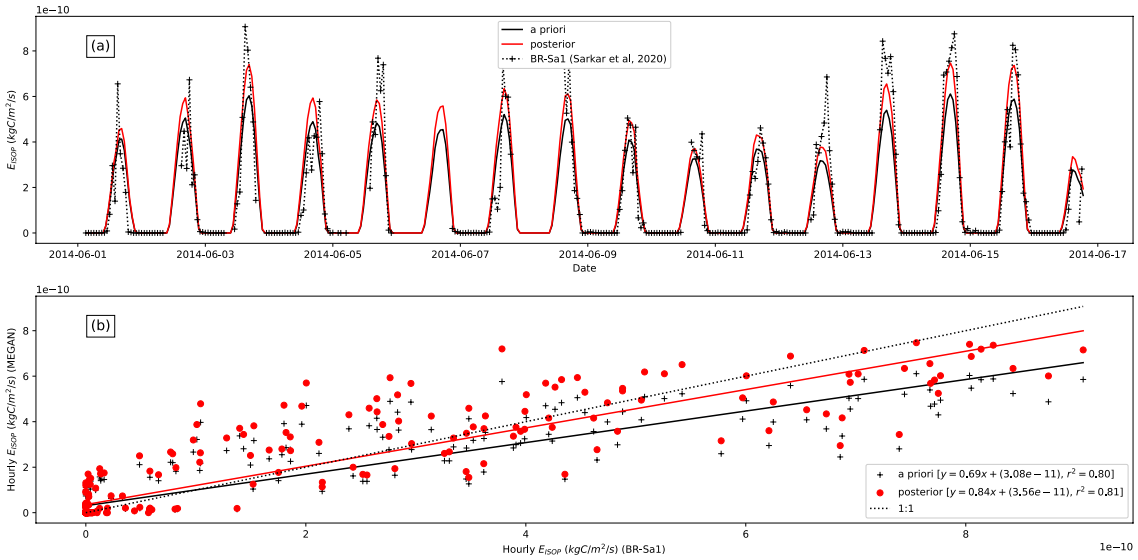

Figure S8. (a) A priori and posterior MEGAN isoprene flux estimates at BR-Sa1 from 1 – 16 June 2014, using the parameter subset of T_{Max} and K_1. The posterior emissions were calculated using the optimized $\boldsymbol{\gamma}_T$ based on eddy covariance observations (+ symbols). The dotted red line denotes the interquartile range on the posterior emission estimate. (b) Correlation between observed and modelled hourly mean isoprene emission rates at BR-Sa1. The solid red line is a

linear fit to the posterior modelled emissions (red circles), whereas the solid black curve is a linear fit to the a priori emissions (+ symbols).

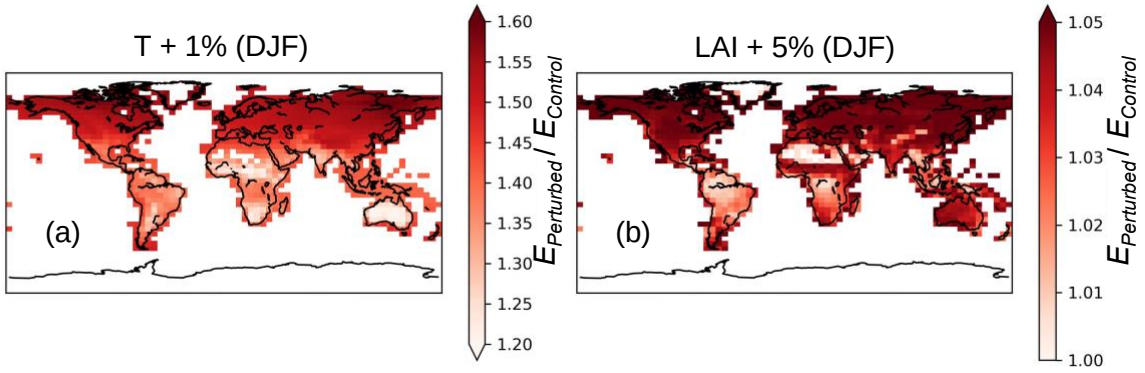

Figure S9. (a) Ratio of the biased ("Perturbed") and unbiased ("Control") seasonally averaged MEGAN isoprene emissions in December-January-February 2016–2017 when running the model with biased (+1%) temperature input data. (b) As in (a) but using biased (+5%) LAI input data. Note the scale of the colour bar in (b) is greatly reduced compared to (a), reflected the lower sensitivity of MEGAN to LAI.

Variable	Description	Standard Value
LAI	Leaf area index	5 cm^2/cm^2
F_{MAT}	Fraction of mature leaves	80%
F_{GRO}	Fraction of growing leaves	10%
F_{OLD}	Fraction of old leaves	10%
φ	Solar elevation angle	60°
τ_{PPFD}	PPFD transmission from top of atmosphere to canopy	0.6
T	Air temperature	303 K
T24	Average air temperature of past 24 hours	297 K
$PPFD_{SUN}$	Photosynthetic photon flux density (Sun leaves)	200 $\mu mol/m^2/s$
$PPFD_{SHADE}$	Photosynthetic photon flux density (shade leaves)	50 $\mu mol/m^2/s$

Table S1. Standard conditions for MEGAN γ-factors as defined by Guenther et al (2006). Under these conditions, isoprene emissions are equal to the standard emission rate ($E_{ISOP} = E_0$). We list here only the standard conditions which appear in the PCEEA implementation of MEGAN. Other standard driving variables, including wind speed and humidity, are only required when using the full MEGAN canopy environment model.

References From the Supporting Information

Barkley, M. P., Smedt, I. D., Van Roozendael, M., Kurosu, T. P., Chance, K., Arneth, A., Hagberg, D., Guenther, A., Paulot, F., Marais, E., & Mao, J. (2013). Top-down isoprene emissions over tropical South America inferred from SCIAMACHY and OMI formaldehyde columns. *Journal of Geophysical Research: Atmospheres*, *118*(12), 6849–6868. https://doi.org/10.1002/jgrd.50552

De Smedt, I., Pinardi, G., Vigouroux, C., Compernolle, S., Bais, A., Benavent, N., Boersma, F., Chan, K.-L., Donner, S., Eichmann, K.-U., Hedelt, P., Hendrick, F., Irie, H., Kumar, V., Lambert, J.-C., Langerock, B., Lerot, C., Liu, C., Loyola, D., Piters, A., Richter, A., Rivera Cárdenas, C., Romahn, F., Ryan, R. G., Sinha, V., Theys, N., Vlietinck, J., Wagner, T., Wang, T., Yu, H., and Van Roozendael, M.: Comparative assessment of TROPOMI and OMI formaldehyde observations and validation against MAX-DOAS network column measurements, Atmos. Chem. Phys., 21, 12561–12593, https://doi.org/10.5194/acp-21-12561-2021, 2021.

Fang, H., Jiang, C., Li, W., Wei, S., Baret, F., Chen, J. M., Garcia-Haro, J., Liang, S., Liu, R., Myneni, R. B., Pinty, B., Xiao, Z., & Zhu, Z. (2013). Characterization and Intercomparison of Global Moderate Resolution Leaf Area Index (LAI) products: Analysis of climatologies and theoretical uncertainties. *Journal of Geophysical Research: Biogeosciences*, *118*(2), 529–548. https://doi.org/10.1002/jgrg.20051

Ferracci, V., Bolas, C. G., Freshwater, R. A., Staniaszek, Z., King, T., Jaars, K., Otu-Larbi, F., Beale, J., Malhi, Y., Waine, T. W., Jones, R. L., Ashworth, K., & Harris, N. R. (2020). Continuous isoprene measurements in a UK temperate forest for a whole growing season: Effects of drought stress during the 2018 heatwave. *Geophysical Research Letters*, *47*(15). https://doi.org/10.1029/2020gl088885

Geron, C., Guenther, A., Sharkey, T., & Arnts, R. R. (2000). Temporal variability in basal isoprene emission factor. *Tree Physiology*, *20*(12), 799–805. https://doi.org/10.1093/treephys/20.12.799

Guenther, A., Karl, T., Harley, P., Wiedinmyer, C., Palmer, P. I., & Geron, C. (2006). Estimates of global terrestrial isoprene emissions using MEGAN (model of emissions of gases and aerosols from nature). *Atmospheric Chemistry and Physics*, *6*(11), 3181–3210. https://doi.org/10.5194/acp-6-3181-2006

Hanson, D. T., & Sharkey, T. D. (2001). Rate of acclimation of the capacity for isoprene emission in response to light and temperature. *Plant, Cell & Environment*, *24*(9), 937–946. https://doi.org/10.1046/j.1365-3040.2001.00745.x

Marais, E. A., Jacob, D. J., Kurosu, T. P., Chance, K., Murphy, J. G., Reeves, C., Mills, G., Casadio, S., Millet, D. B., Barkley, M. P., Paulot, F., & Mao, J. (2012). Isoprene emissions in Africa inferred from OMI observations of formaldehyde columns. *Atmospheric Chemistry and Physics*, *12*(14), 6219–6235. https://doi.org/10.5194/acp-12-6219-2012

Millet, D. B., Jacob, D. J., Turquety, S., Hudman, R. C., Wu, S., Fried, A., Walega, J., Heikes, B. G., Blake, D. R., Singh, H. B., Anderson, B. E., & Clarke, A. D. (2006). Formaldehyde distribution over North America: Implications for satellite retrievals of formaldehyde columns and isoprene emission. *Journal of Geophysical Research*, *111*(D24). https://doi.org/10.1029/2005jd006853

Monson, R. K., Harley, P. C., Litvak, M. E., Wildermuth, M., Guenther, A. B., Zimmerman, P. R., & Fall, R. (1994). Environmental and developmental controls over the seasonal pattern of isoprene emission from Aspen leaves. *Oecologia*, *99*(3-4), 260–270. https://doi.org/10.1007/bf00627738

Palmer, P. I., Jacob, D. J., Fiore, A. M., Martin, R. V., Chance, K., & Kurosu, T. P. (2003). Mapping isoprene emissions over North America using formaldehyde column observations from space. *Journal of Geophysical Research: Atmospheres*, *108*(D6). https://doi.org/10.1029/2002jd002153

Pétron, G., Harley, P., Greenberg, J., & Guenther, A. (2001). Seasonal temperature variations influence isoprene emission. *Geophysical Research Letters*, *28*(9), 1707–1710. https://doi.org/10.1029/2000gl011583

Sarkar, C., Guenther, A. B., Park, J.-H., Seco, R., Alves, E., Batalha, S., Santana, R., Kim, S., Smith, J., Tóta, J., & Vega, O. (2020). PTR-TOF-MS eddy covariance measurements of isoprene and monoterpene fluxes from an eastern Amazonian rainforest. *Atmospheric Chemistry and Physics*, *20*(12), 7179–7191. https://doi.org/10.5194/acp-20-7179-2020

Stavrakou, T., Müller, J.-F., Bauwens, M., De Smedt, I., Van Roozendael, M., De Mazière, M., Vigouroux, C., Hendrick, F., George, M., Clerbaux, C., Coheur, P.-F., & Guenther, A. (2015). How consistent are top-down hydrocarbon emissions based on formaldehyde observations from GOME-2 and OMI? *Atmospheric Chemistry and Physics*, *15*(20), 11861–11884. https://doi.org/10.5194/acp-15-11861-2015

Turner, A. J., Henze, D. K., Martin, R. V., & Hakami, A. (2012). The spatial extent of source influences on modeled column concentrations of short-lived species. *Geophysical Research Letters*, *39*(12). https://doi.org/10.1029/2012gl051832

Vigouroux, C., Langerock, B., Bauer Aquino, C. A., Blumenstock, T., Cheng, Z., De Mazière, M., De Smedt, I., Grutter, M., Hannigan, J. W., Jones, N., Kivi, R., Loyola, D., Lutsch, E., Mahieu, E., Makarova, M., Metzger, J.-M., Morino, I., Murata, I., Nagahama, T., … Winkler, H. (2020). Tropomi–sentinel-5 precursor formaldehyde validation using an extensive network of ground-based Fourier-transform infrared stations. *Atmospheric Measurement Techniques*, *13*(7), 3751–3767. https://doi.org/10.5194/amt-13-3751-2020

Wolfe, G. M., Kaiser, J., Hanisco, T. F., Keutsch, F. N., de Gouw, J. A., Gilman, J. B., Graus, M., Hatch, C. D., Holloway, J., Horowitz, L. W., Lee, B. H., Lerner, B. M., Lopez-Hilifiker, F., Mao, J., Marvin, M. R., Peischl, J., Pollack, I. B., Roberts, J. M., Ryerson, T. B., … Warneke, C. (2016). Formaldehyde production from isoprene oxidation across NOx regimes. *Atmospheric Chemistry and Physics*, *16*(4), 2597–2610. https://doi.org/10.5194/acp-16-2597-2016